Fluidized Bed Combustion of Liquid Biofuels: Application of Integrated Diagnostics for Micro-explosions Characterization

L. Ferrante,[†] M. Miccio,*[,†] F. Miccio,[‡] and R. Solimene[‡]

Dipartimento di Ingegneria Chimica e Alimentare, Università di Salerno, via Ponte Don Melillo, I-84084 Fisciano (SA), Italy, and Istituto di Ricerche sulla Combustione, CNR Piazzale V. Tecchio, 80, 80125 Napoli, Italy

Received April 8, 2008. Revised Manuscript Received July 25, 2008

A novel integrated diagnostic technique has been developed for the analysis of the "regime with micro-explosions" that may be established during the low-temperature (T < 800 °C) fluidized bed combustion of liquid fuels. It consists of the comparison among three analogue data series: (i) pressure signals measured in the freeboard and high-pass filtered, (ii) oxygen molar fractions measured by zirconia-based probes at two elevations in the bed and in the splash region, and (iii) video frames of the bed surface recorded and purposely worked out. The integrated technique has been applied to the combustion of biodiesel at minimum fluidization and has proven to be a valid tool to provide the fingerprints of the mechanism of the low-temperature fluidized combustion of liquid fuels. The time series generated from the measured data sets have been analyzed with the aid of the Hurst's rescaled range analysis, the V-statistic, and the Lyapunov exponents' evaluation. The issue of localizing micro-explosions throughout bed, bubbles, and splash zone has been tackled by the V-statistic analysis, which has proven that the location of micro-explosions is just at the bed surface when $T = 650$ °C and moves deeper and deeper into the bed when its temperature increased to about 800 °C. The values found for the largest Lyapunov exponent in the time series demonstrate that the investigated system is not only dynamic but also chaotic in its nature.

Introduction

Fluidized bed is a suitable technology for difficult to burn liquid fuels, such as oil refinery wastes, used mineral oils, vegetable and pyrolysis oils from biomass, as well as food-derived sludge, thanks to the its robustness, flexibility, and effectiveness.[1] In contrast, conventional stationary combustion applications for power production or industrial- and small-scale heat generation require pre-processing treatments for the above fuels, e.g., the transesterification process for upgrading vegetables oils to biodiesel or refining for biomass/waste pyrolysis oils.[2]

Differently from a combustible gas, a conventional liquid fuel cannot be easily premixed with the air feed in a fluidized bed. Whatever the means and the position that a liquid fuel is fed to the fluidized bed, a prerequisite to its combustion is that the fuel could be dispersed into the bed and brought into contact with oxygen, i.e., with the fluidizing and secondary air. Once injected into a hot bed, liquid fuels form agglomerates with the particles of the hot bed;[3,4] however, as a consequence of the direct contact with the high-temperature solids, rapid fuel vaporization and pyrolysis develops. In the case of in-bed air-assisted fuel injection, the liquid vaporization starts inside a submerged jet; thus, bubbles generated by the periodical collapse of the jet are rich in fuel vapors. Miccio et al.[5] extended the concept of "endogenous" bubbles proposed by Fiorentino et al.[6] for high-volatile solid fuels to the fuel-generated vapor bubbles, whereas the air bubbles generated past the distributor are classified as "exogenous". While the endogenous bubbles are rising along the bed, they earn oxygen by diffusion from the emulsion phase and by coalescence with air-rich exogenous bubbles. In such a situation, an endogenous bubble is expected to enter within the flammability limits for the hydrocarbons that it contains, and if a condition for ignition occurs, it undergoes partial or total burn off. Experiments seem to prove that the conversion of fuel vapors is limited to the bubble phase or the freeboard.[7,8] Quenching of combustion inside the bed emulsion was attributed mainly to the recombination of radicals on the large surface area of the inert bed particles.[9] The overall combustion efficiency inside the bed is then strictly related to the fate of the endogenous bubbles. Diffusive flames take place above the bed as soon as fuel-rich pockets are released and ignited. These flames have a transient behavior, a short life, and sometimes are the result of a micro-explosion. All factors that contribute to lower fuel conversion in the bed and to defer combustion to the freeboard represent a perturbation with respect to an idealized combustion process in which all chemical and thermal steps are confined to the bubbling bed only.

* To whom correspondence should be addressed. Fax: +39-089-964057. E-mail: mmiccio@unisa.it.

[†] Università di Salerno.

[‡] Istituto di Ricerche sulla Combustione.

(1) Saxena, S. C.; Jotshi, C. K. *Prog. Energy Combust. Sci.* **1994**, *20*, 281–324.

(2) Czernik, S.; Bridgwater, A. V. *Energy Fuels* **2004**, *18*, 590–598.

(3) Ariyapadi, S.; Holdsworth, D. W.; Norley, C. J. D.; Berruti, F.; Briens, C. *Int. J. Chem. Reactor Eng.* **2003**, *1*, A56.

(4) Bruhns, S.; Werther, J. *AIChE J.* **2005**, *51*, 766–775.

(5) Miccio, F.; Miccio, M.; Olivieri, G. Proceedings of 16th International Conference on Fluidized Bed Combustion, American Society of Mechanical Engineers (ASME), New York, 2001; pp 1076−1099.

(6) Fiorentino, M.; Mazzocchella, A.; Salatino, P. *Chem. Eng. Sci.* **1997**, *52*, 1893–1908.

(7) Dennis, J. S.; Hayhurst, A. N.; Mackley, I. J. *Proc. Combust. Inst.* **1982**, *19*, 1205–1212.

(8) van der Vaart, R. D. *Combust. Flame* **1988**, *71*, 35–39.

(9) Hayhurst, A. N. *Combust. Flame* **1991**, *85*, 155–168.

10.1021/ef800246w CCC: $40.75
Published on Web 09/13/2008

The application of pressure or acoustic probes to fluidized beds is a well-established technique for characterizing the bed fluid dynamics.[10] Acoustic signals generated during premixed FB combustion of gaseous hydrocarbons were taken into consideration and comprehensively investigated by Zukowski.[11,12] Transient pressure profiles were recorded, showing a huge distribution of pressure peaks that were attributed to explosions. The analysis demonstrated that the combustor exhibited an explosive behavior in a large temperature range. Zukowski[13] individuated three ranges of bed temperature within which different combustion regimes occur when burning mixtures of methane and air in a bubbling fluidized bed of inert particles. These ranges are (A) with $T_{bed} < T_{cr1}$, the gases burn continuously above the bed, which is cooler than freeboard; (B) when $T_{cr1} < T_{bed} < T_{cr2}$, combustion moves into the bed, becomes intermittent, and takes place in an explosive manner in bubbles reaching or approaching the bed surface; and (C) at the highest temperatures, with $T_{bed} > T_{cr2}$, the bubbles explode inside the bed at a distance from the distributor depending upon the induction period for the thermal ignition of the combustible mixture. Furthermore, Bulewicz et al.[14] introduced a technique based on video recordings of the bed and on image analysis in three color bands to investigate the explosive behavior in the laboratory-scale, premixed combustion of methane. In the above cases, also zirconia-based solid-state sensors turn out useful. They have been used in fluidized beds by a number of investigators[15−18] whenever information concerning spatial or dynamic changes of the oxygen concentration is relevant for understanding the process phenomena. By means of zirconia-based sensors with fast time response, Solimene et al.[19] investigated gas mixing phenomena inside the bed as well in the splash zone with high accuracy and time resolution.

The goal of this work is the application of a novel integrated diagnostic technique for the analysis of the "regime with micro-explosions" that Miccio et al.[20] demonstrated may be established during the low-temperature fluidized bed combustion of liquid fuels. This new technique is based on simultaneous measurements of oxygen concentration by zirconia-based probes in the bed and splash region, pressure signals in the freeboard, and video-recordings of the bed surface. The technique was directed at exploiting the mechanism of the low-temperature ($T < 800$ °C) fluidized combustion of liquid fuels, with special attention toward the issue of localizing micro-explosions throughout bed, bubbles, and splash zone.

Experimental Section

Experimental Apparatus. An atmospheric bubbling fluidized bed reactor (FBR140) sketched in Figure 1 has been used for experiments of steady-state combustion of liquid fuels. The fluidization column is formed by two cylindrical AISI 316 stainless-steel tubes having different sizes, 140 and 200 mm i.d., respectively. A conical section is mounted to permit a gradual change of size between the tubes. The first tube (1010 mm high) has an inside diameter $d_t = 140$ mm and contains the bed and the splash zone; the second one (1800 mm high) is the disengaging section. The reactor can work at operating temperatures up to 900 °C thanks to electrical heating that is supplied by radiant shells installed along the fluidization column for a total height of 2 m. The fluidizing gas can be preheated up to 500 °C and then fed to an air plenum. The air distributor consists of a reversed cone filled with stainless-steel (AISI 304) $^3/_8''$ spheres to even the flow out. A cyclone is fitted at the exit of the reactor.

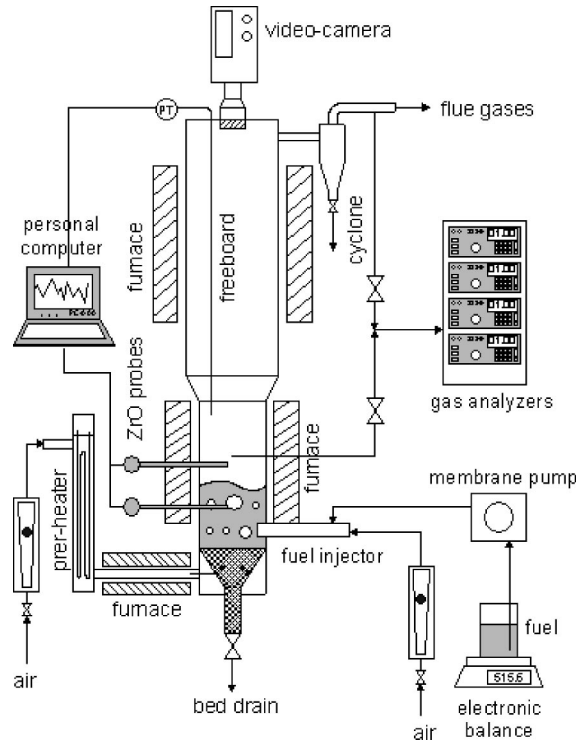

Figure 1. Schematic representation of the FBR140 experimental facility.

The liquid fuel was metered by means of a membrane pump (KNF Stepdos type). The mass flow rate was determined by the mass variation of the fuel vessel mounted on a high-accuracy digital balance. A horizontal fuel injector was wall-positioned and located at a height of 140 mm above the flange between the reversed cone and the fluidization column. It was water-cooled, air-assisted, and fitted with a 2 mm i.d. terminal nozzle. The flow rates of the fluidizing gas and the dispersion air were measured by rotameters.

Diagnostics. The freeboard pressure was measured by a transducer (Druck PTX type, 0−100 mbar range, 1 kHz maximum sampling rate), characterized by a fast time response and high sensibility, and connected to the freeboard by means of a waveguide made by a 6 mm i.d. and 2.5 m long stainless-steel tube. This setup allowed for dynamic pressure measurements at a height of 1 m above the air distributor. The pressure signals were acquired by a data acquisition unit coupled with a PC.

Flue gases were continuously sampled at the stack and passed in sequence through a filter, a heated tube, a cooling unit, a pump, and finally, a battery of gas analyzers for O_2, CO_2, CO, N_2O, NO_x, and CH_4.

The fluidization column was also equipped with three zirconia-based probes (SIRO2 C700 + DS probe) to measure the oxygen concentration along the reactor. The adopted oxygen solid-state sensor is custom-made, and it is characterized by a zirconia-based cylindrical pellet, 4 mm diameter and 3 mm long, sealed at the end of a 6 mm diameter alumina tube. Air is continuously fed as reference gas to the inner surface of the zirconia pellet. A R-type

(10) Johnsson, F.; Zijerveld, R. C.; Schouten, J. C.; van den Bleek, C. M.; Leckner, B. *Int. J. Multiphase Flow* **2000**, *26*, 663–715.
(11) Zukowski, W. *Combust. Flame* **1999**, *117*, 629–635.
(12) Zukowski, W. *Combust. Flame* **2002**, *130*, 15–26.
(13) Zukowski, W. *Combust. Flame* **2003**, *134*, 399–409.
(14) Bulewicz, E. M.; Zukowski, W.; Kandefer, S.; Pilawska, M. *Combust. Flame* **2003**, *132*, 319–327.
(15) Ljungstroem, B. Proceedings of the 8th International Conference on Fluidized Bed Combustion, American Society of Mechanical Engineers (ASME), New York, 1985; pp 853−864.
(16) Sterneus, J.; Johnsson, F.; Leckner, B.; Wiesendorf, V.; Werther, J. *J. Inst. Energy* **2000**, *73*, 184–190.
(17) Stubington, J. F.; Chan, S. W. *J. Inst. Energy* **1990**, *63*, 136–142.
(18) Stubington, J. F.; Clough, S. J. Proceedings of the 14th International Conference on Fluidized Bed Combustion; American Society of Mechanical Engineers (ASME), New York, 1997; pp 1111−1122.
(19) Solimene, R.; Marzocchella, A.; Pessarelli, G.; Salatino, P. *AIChE J.* **2006**, *52*, 185–198.
(20) Miccio, F.; Miccio, M.; Olivieri, G.; Silvestre, A. *Ind. Eng. Chem. Res.* **2003**, *42*, 3973–3981.

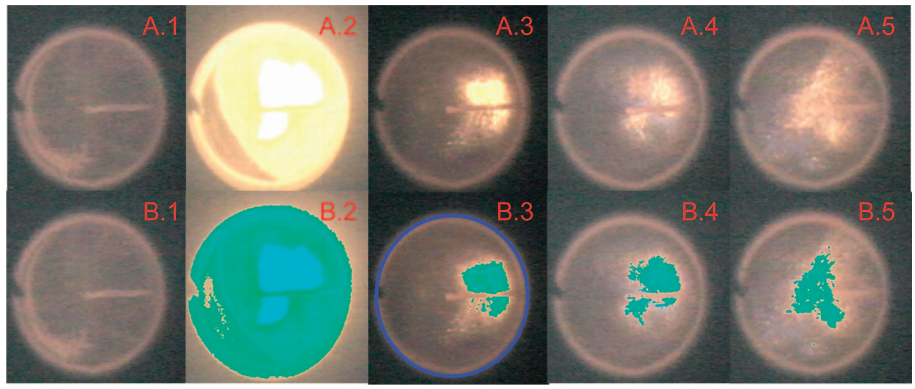

Figure 2. Sequence of frames representing the bed surface recorded from the top of the fluidization column during the occurrence of a micro-explosion (fuel, biodiesel; sand size, 200−400 μm; T, 650 °C; u_0, 100 m/s; U, 0.25 m/s; bottom fuel injection; frame rate, 25 fps). (A) Series, original frames. (B) Series, frames elaborated with the MatLab program.

frame number	B.1	B.2	B.3	B.4	B.5
Ψ values	0.00	0.81	0.055	0.061	0.069

thermocouple is kept in touch with the inner surface of the zirconia pellet to measure the sensor tip temperature. An electromotive force, V, is generated when the two sensor tip surfaces are exposed to gases at different oxygen concentrations. The signals of the oxygen solid-state sensors have been elaborated according to Solimene et al.[19] in light of a Nernst-like equation that relates the electromotive force, V, to the oxygen molar fraction in the investigated gas

$$V = V_{\text{ref}} - \frac{RT}{4F}\ln\left(\frac{y_{O_2}}{y_{O_2,\text{ref}}}\right) \quad (1)$$

where R, T, F, y_{O_2}, $y_{O_2,\text{ref}}$, and V_{ref} are the ideal gas constant, the sensor tip temperature, the Faraday constant, the oxygen molar fraction in the investigated gas and the reference gas, and the electromotive force corresponding to $y_{O_2} = y_{O_2,\text{ref}}$, respectively. The digit 4 accounts for the number of electrons involved in the electrochemical reactions.

The small size of the sensor tip determined a response time lower than 10 ms, following a change in the oxygen concentration. The sensors were horizontally mounted in the bottom section of the fluidization column to position the sensor tips along the column axis at a height of 30, 330, and 480 mm above the distributor level, respectively. The simultaneous acquisition of sensor tip temperature and electromotive force allowed for the estimation of the instantaneous oxygen molar fraction. The corresponding values were acquired by a data acquisition unit coupled with a PC.

An optical window on the top of the fluidization column allowed for the bed surface to be filmed by a PAL video camera (with a frame rate up to 30 fps). The analogical output of this latter was sent to a TV card, suitably digitalized, and saved as a PC file. A computer program, which was developed ad-hoc in MatLab, allowed for the digitalized video file to be worked out. The program examines the video file frame by frame, encircles the bed surface, and counts the number of pixels in each frame that exhibit luminosity above a given threshold. Finally, for each frame, it calculates a luminosity index Ψ, which has the meaning of the fraction of the bed cross-sectional area involved in a micro-explosion or flame at the corresponding time. A new time series was generated in such a way with its own sampling period and made available for an integrated comparison to those concerning the freeboard pressure and O_2 concentrations.

The overall data management with PC allowed for full synchronization of all of the time series generated from the originally acquired signals, i.e., pressure, oxygen molar fractions, and luminosity index.

Materials. Silica sand with a 200−400 and 620−850 μm size range was used as bed material. The minimum fluidization velocity (experimentally evaluated at 650 °C) is $U_{\text{mf}} = 0.049$ and 0.20 m/s, respectively. The bed mass was 7 kg, corresponding to a static bed height $H_{\text{mf}} = 300$ mm and a bed aspect ratio, H_{mf}/d_t, of about 2.1. The liquid fuel was a commercial biodiesel from Novaol, Italy.

Experimental Procedure. When the fluidized bed reaches the temperature of about 500 °C by external heating, fuel feeding into the reactor is started. The flow rates of the various streams, i.e., air and liquid fuel, are adjusted to achieve the desired regime condition. Temperatures, pressures, freeboard, and flue gas concentrations are online-monitored and recorded at 1000 Hz by the data acquisition software written in LabView 7.0. Typically, once the steady-state condition of the preset combustion test is reached, all of the measured variables are acquired for at least 30 min.

Two different hold-ups of spheres in the reverse cone used as an air distributor are adopted to obtain two different elevations of fuel injection with respect to the fluidization air distribution level, i.e., 12 and 140 mm, respectively. These two positions will be referred to as "bottom injection" and "upper injection", respectively, in the present paper.

Experiments were carried out by fixing a value of the bed temperature, T, in the range of 600−800 °C. The finer sand and bubbling conditions (i.e., $U \gg U_{\text{mf}}$) with $U = 0.25$ m/s were used in the tests aimed at characterizing the low-temperature combustion phenomenology; the coarser sand and minimum fluidization conditions (again with $U = 0.25$ m/s) were used in the tests aimed at testing the integrated diagnostic technique. The overall air excess was kept constant at $e = 1.27$ to achieve an oxygen molar fraction in the flue gas of about 5%. The dispersion air velocity at the fuel nozzle was $u_0 = 100$ m/s. Correspondingly, the estimated length of the two-phase air-fuel jet was in the range 20−30 mm; the jet bubble size was about 50 mm; the jet bubble frequency was about 6 Hz; and the calculated jet air/fuel mass ratio was about 5.

It is worth noting that the operating value adopted for U is comprehensive of both fluidizing air at the distributor and dispersion air at the injector.

Results

Phenomenology. Figure 2 reports a typical sequence of frames acquired by the video camera at 25 fps during the interval of a micro-explosive event under bubbling conditions (200−400 μm sand, $U = 0.25$ m/s) and bottom injection of biodiesel at $T = 650$ °C and $u_0 = 100$ m/s. The original sequence of frames is shown in Figure 2A as captured by the video camera. The darker areas represent the emulsion phase, whereas the brighter ones correspond to light-emitting flames. Figure 2A.2 displays a light flash (yellow-colored area) that extends to almost the entire bed surface, whereas the next three snapshots (A.3−A.5 of Figure 2) show its rapid extinction. The occurrence of the light flash is followed by a marked pressure peak as revealed by the transducer in the freeboard and demonstrated by the

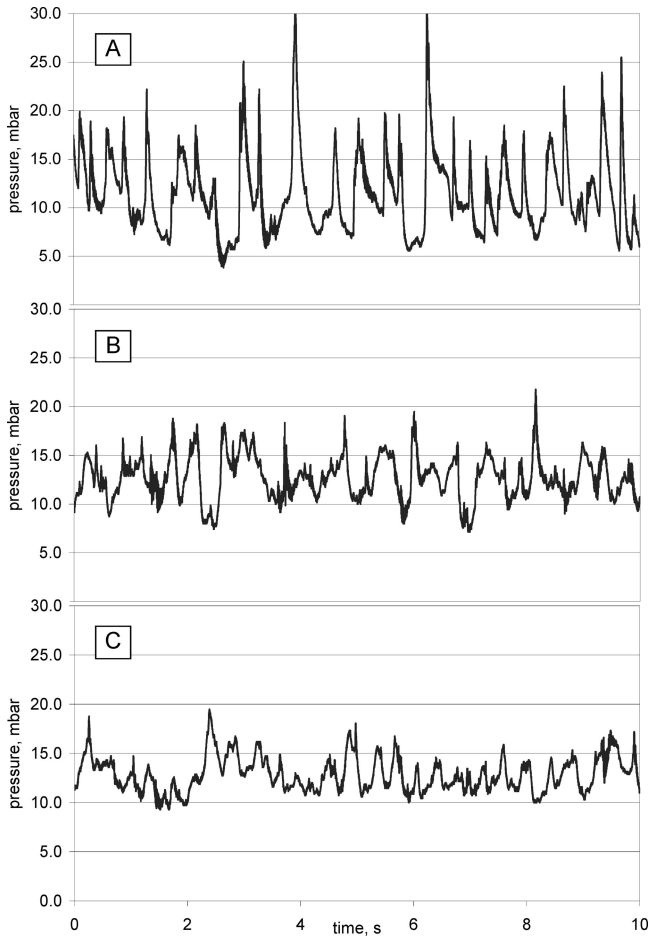

Figure 3. Time-resolved pressure profiles in the freeboard at different bed temperatures: (A)$T = 600$ °C, (B)$T = 650$ °C, and (C)$T = 700$ °C (fuel, biodiesel; sand size, 200−400 μm; u_0, 100 m/s; U, 0.25 m/s; bottom fuel injection).

pressure pattern in Figure 3. The sudden pressure increase generates an acoustic wave in the cylindrical vessel that is smoothed in a short time. The ensemble of these events is referred to as micro-explosion.

In general, there is evidence that a single micro-explosion does not cover the entire bed section and seems to begin below the bed surface. Events of this kind are very frequent in the video recordings and can be considered typical of the combustion behavior of liquid fuels under the operating conditions of the present study. Therefore, we obtained a further confirmation on a larger scale of the same combustion "regime with micro-explosions" that was previously observed by Miccio et al.[20] at the laboratory scale. The results are also in agreement with the phenomenology described in details by Bulewicz et al.,[14] with reference to the premixed combustion of methane in a laboratory-scale bubbling fluidized bed.

Actually, two sequences of frames are reported in Figure 2, with the second one (B) being an example of how the MatLab code manipulated the same series of frames (A). The pixels that exhibited a luminosity above a given threshold, as recognized by the program, were marked in green (Figure 2B). The sequence of values calculated for the luminosity index Ψ, as reported in the caption of Figure 2, provides a quantitative evidence of the previous image-based qualitative discussion of the five frames in Figure 2A.

Figure 3 shows three time profiles of the freeboard pressure obtained at increasing bed temperatures, i.e., $T = 600$, 650, and 700 °C. They exhibit characteristic pressure spikes that suddenly

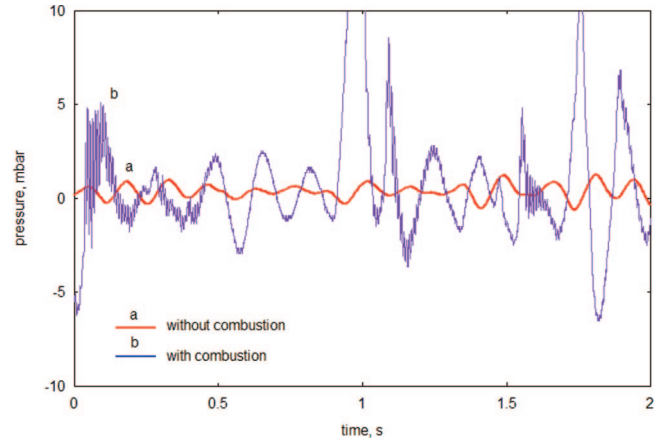

Figure 4. Pressure signals acquired during tests without (a) and with (b) fuel feeding under bubbling conditions in air (fuel, biodiesel; sand size, 200−400 μm; T, 600 °C; $U - U_{mf}$, 0.2 m s^{-1}; u_0, 100 m s^{-1}).

detach above the base level of pressure with certain regularity in the observed time window. Each spike is quickly smoothed down, while other smaller amplitude, higher frequency fluctuations are superimposed to it. The average height of the pressure spikes decreases with increasing temperature, as one may clearly note when moving from A to C in Figure 3. Above $T = 800$ °C, the micro-explosive behavior disappears and the pressure pattern becomes much smoother.

For a comparison, Figure 4 reports the freeboard pressure time profiles acquired during two tests that were carried out under bubbling conditions and with a constant bed temperature ($T = 600$ °C) without any fuel (curve a) and with fuel feeding (curve b), respectively. A stream of dispersion air was fed to the nozzle with $u_0 = 100$ m/s in both tests. The curve a in Figure 4 exhibits the small-amplitude, low-frequency fluctuations typically induced by the eruption of the air bubbles at the bed surface. It is clear that the pressure fluctuations because of the hydrodynamic behavior of a bubbling fluidized bed (curve a) are significantly amplified during the test carried out with fuel injection and consequent combustion (curve b). This is due to a lesser extent to the volume expansion of the bubbles upon fuel evaporation and combustion; more importantly, it is a consequence of the occurrence of micro-explosions, which were clearly detected during such a test (curve b in Figure 4b). As a further confirmation, the acoustic waves produced by micro-explosions are evident along curve b, as superimposed oscillations with higher characteristic frequencies.

When using pressure data in the integrated diagnostics technique, the original pressure signals were processed by a high-pass filter with a cut frequency of 80 Hz to remove pressure fluctuations induced by the bubbling bed and to highlight the acoustic component of the signal following a micro-explosion. This component has a frequency of 115 Hz at $T = 600$ °C that compares well to the theoretical value $c/2L_t = 118$ Hz of the resonance frequency for a semi-closed tube having a length $L_t = 2.5$ m.

Phenomenology and results discussed thus far remained substantially the same irrespective of bottom or upper injection of the liquid fuel. It should be remarked here that bottom injection is by far preferable in fluidized bed combustion of liquid fuels.[1]

The Hurst analysis[21,22] has been applied to the time series of the original pressure data acquired in the freeboard. In particular,

(21) Ferrante, L. Ph.D. Thesis; Department of Chemical and Food Engineering, University of Salerno, Italy, 2007.

(22) Peters, E. E. *Applying Chaos Analysis to Investment and Economics*; Wiley: New York, 1994.

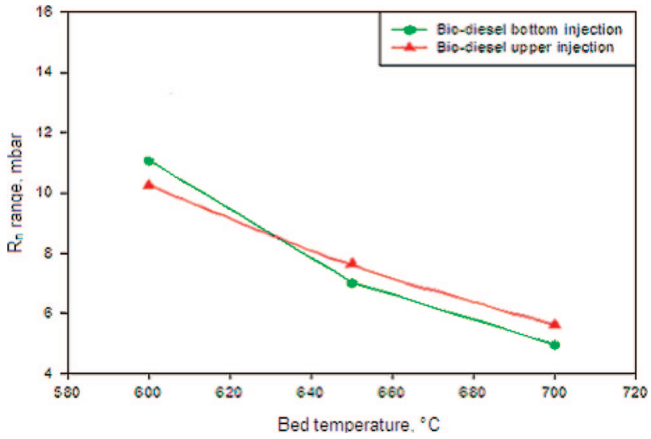

Figure 5. Average amplitude ranges R_n evaluated at different bed temperatures in correspondence of the characteristic cycle time of the freeboard pressure signals (sand size, 200−400 μm; u_0, 100 m/s; U, 0.25 m/s).

Table 1. Relevant Gas Concentrations Measured at the Combustor Exit[a]

test number	T (°C)	O_2 (%)	CO_2 (%)	CO (ppm)	CH_4 (ppm)
1	650	5.19	12.59	55.23	57
2	700	4.87	12.05	63.21	6
3	750	5.01	12.04	32.02	7
4	800	5.22	11.86	14.52	10

[a] Operating conditions: fuel, biodiesel; sand size, 0.62−0.85 mm; U, 0.25 m/s; u_0, 100 m/s; expanded bed height, 400 mm.

the average signal amplitude ranges R_n have been evaluated in correspondence to the break of the $\log_{10}-\log_{10}$ plot of $(R/S)_n$ versus τ_n, as detailed in the Appendix. In Figure 5, the R_n values are reported for combustion tests of biodiesel as a function of the bed temperature for bottom and upper injection; they confirm that the amplitude of the pressure fluctuations decreases with an increasing bed temperature. In turn, this underlines that during the low-temperature combustion of liquid fuels the average intensity of the micro-explosions decreases with an increasing bed temperature.

Integrated Diagnostics. To apply the integrated diagnostics, the minimum fluidization conditions were purposely adopted, so that any possible interference because of the exogenous bubbles in the bed could be avoided in the results. In addition, given the insensitivity of the observed phenomenology to the fuel nozzle position, bottom injection has been adopted.

Table 1 reports the relevant gas concentrations measured at the combustor exit corresponding to four typical tests carried out, feeding the biodiesel in beds at minimum fluidization condition. The time-averaged values of the flue gas composition during the desired regime condition were determined for different bed temperatures. It is worth to note that the combustion of biodiesel is substantially complete in all of the tests, even if CO and CH_4 emissions decrease with increasing bed temperature.

Figure 6 shows the results relative to the combustion test at $T = 650$ °C. The oxygen concentration profile measured in the splash zone, i.e., at 80 mm above the bed surface, is reported in Figure 6B. The diagram clearly highlights noticeable fluctuations. The average value of the O_2 molar fraction in the observed time window is about 6%, but sometimes the concentration abruptly decreases. These sudden drops in the oxygen concentration denote the passage of oxygen-starving pockets in the splash zone, meaning that mixing has not occurred between partial or complete combustion products (including those generated by micro-explosions) coming from fuel bubbles and the excess air coming from the emulsion phase.

The time-resolved oxygen concentration diagram measured inside the bed, i.e., 70 mm below the bed surface, is shown in Figure 6D. The average value is 2%, i.e., considerably lower than that of the flue gas. The instantaneous O_2 molar fraction is lower than 1% for the most of the time but reaches peaks as high as 9% in some instances. This trend is due to the particular operating condition of the bed, with the dense phase at minimum fluidization. Very likely, a train of fuel bubbles forms downstream from the injector, and each bubble rises vertically along the bed axis. Therefore, the zirconia-based sensor tip spends most of the measuring time within fuel bubbles, i.e., under O_2-starving conditions.

The high-pass filtered component of the pressure time series measured in the freeboard (Figure 6C) highlights the occurrence of micro-explosive events with their intensity and frequency. The vertical lines, plotted in parts A−D of Figure 6, mark the time instants corresponding to the detection of a micro-explosion by the start-up of a new, quickly smoothed pressure wave. Figure 6E shows a sequence of frames with the light flashes following the first micro-explosion detected in Figure 6C at the time $t = 10.7$ s.

We remark that (i) the pressure measurement technique does not allow for the spatial location of the micro-explosions to be exactly recognized and (ii) events occurring deep in the bed are likely to be promptly smoothed and, consequently, undetectable. To identify the location of micro-explosions, the comparison of the high-pass filtered pressure signal to the luminosity index Ψ and oxygen diagram can be useful. Ψ is in most cases lower than 0.4 (Figure 6A), meaning that a single micro-explosion or a flame visualized in the splash region always covers only a part of the bed section.

Generally, the occurrence of a micro-explosion, as detected by the pressure signal analysis, is accompanied in a very short time span by an increase of Ψ (Figure 6A) and, in most cases, by a sudden drop of the O_2 measurement below the bed surface (Figure 6D). This would suggest that under the conditions tested the micro-explosion starts just below the bed surface. On the other hand, the luminosity index is seldom approaching zero; in particular, $\Psi > 0$ in the observed time window also when a micro-explosion is not detected. This suggests that postcombustion occurs in the splash region under these operating conditions as a luminous flame without the generation of a pressure peak.

The comparison of Figures 6−9 shows that, when the bed temperature is raised, the values of Ψ decrease progressively, the peaks of the filtered pressure signals become less frequent and intense, and the O_2 profiles in the splash zone smooth progressively, with less frequent concentration drops. For a bed temperature higher than 750 °C, the peaks of the filtered pressure signals disappear at all. In particular, when moving from Figures 6A to 9A, the peaks of the luminosity index become less frequent and strong, meaning that the flashes in the splash region are rarer and cover a smaller area. This trend is also confirmed by a simple qualitative analysis of the video snapshots from Figure 6E to 9E. Altogether, the above observations confirm that, in the bed temperature range of 650−800 °C, a shift occurs in the mechanism under investigation, displacing the combustion deeper and deeper inside the bed and making the bed itself able not only to

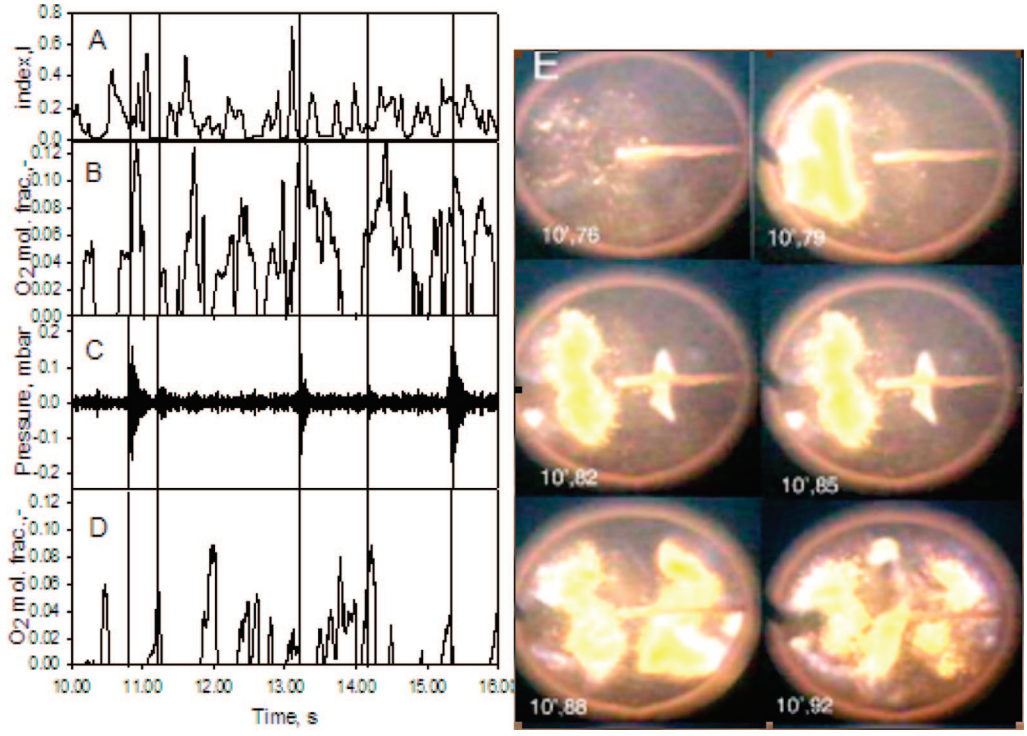

Figure 6. Time-resolved pressure, oxygen concentration, and luminosity index signals and sequence of frames (test 1, $T = 650$ °C): (A) luminosity index Ψ, (B) O_2 concentration in the splash zone, (C) high-pass filtered pressure in the freeboard, (D) O_2 concentration in the bed, and (E) sequence of frames representing the bed surface.

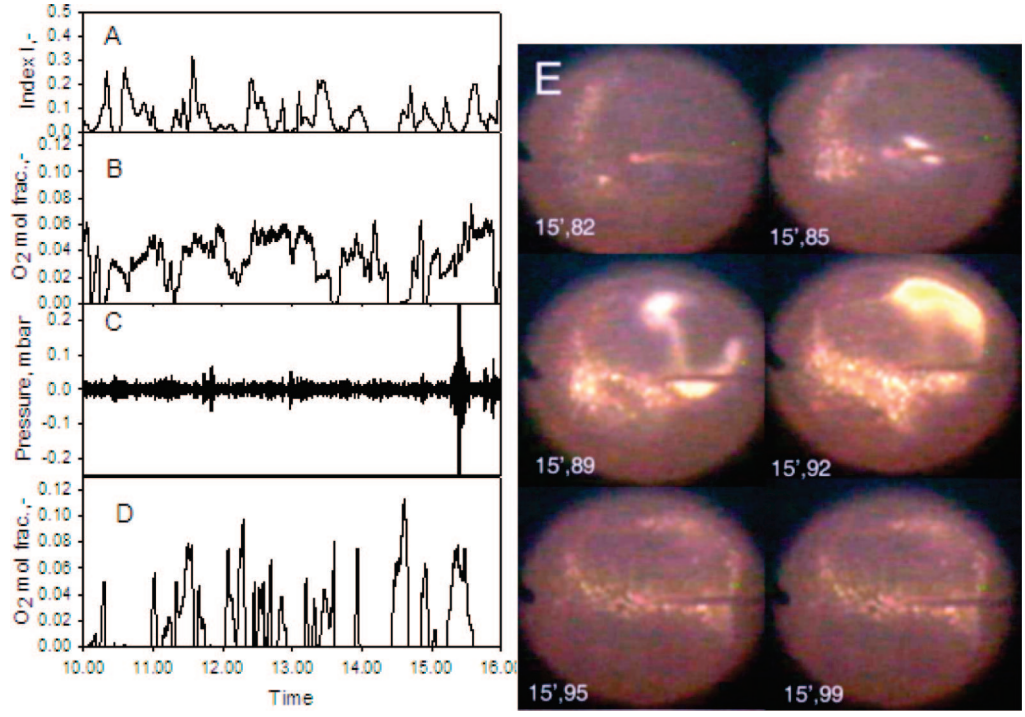

Figure 7. Time-resolved pressure, oxygen concentration, and luminosity index signals and sequence of frames (test 2, $T = 700$ °C): (A) luminosity index Ψ, (B) O_2 concentration in the splash zone, (C) high-pass filtered pressure in the freeboard, (D) O_2 concentration in the bed, and (E) sequence of frames representing the bed surface.

generate chemical species by fuel vaporization and pyrolysis but also to oxidize them.

Discussion

In the above section, a qualitative analysis of the signals was carried out based on the comparison of a very small portion of the acquired data series, i.e., a time window of 6 s. The previous analysis is only applicable to small data sets; to study the mean behavior of the fluidized bed as a combustion reactor, more complex signal analyses have to be taken into consideration. To this end, we have taken into consideration four different time series, each one containing 100 000 points of pressure, O_2 molar fraction, and luminosity index, which were originated from data acquired throughout a time window of 100 s during each of the above-mentioned minimum fluidization tests.

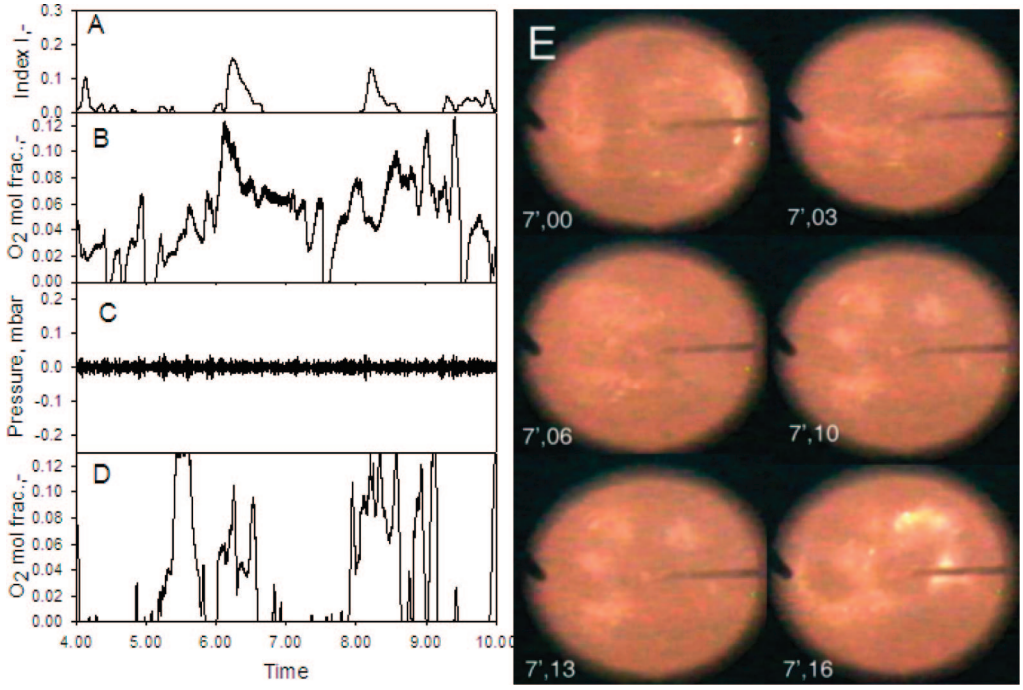

Figure 8. Time-resolved pressure, oxygen concentration, and luminosity index signals and sequence of frames (test 3, $T = 750$ °C): (A) luminosity index Ψ, (B) O_2 concentration in the splash zone, (C) high-pass filtered pressure in the freeboard, (D) O_2 concentration in the bed, and (E) sequence of frames representing the bed surface.

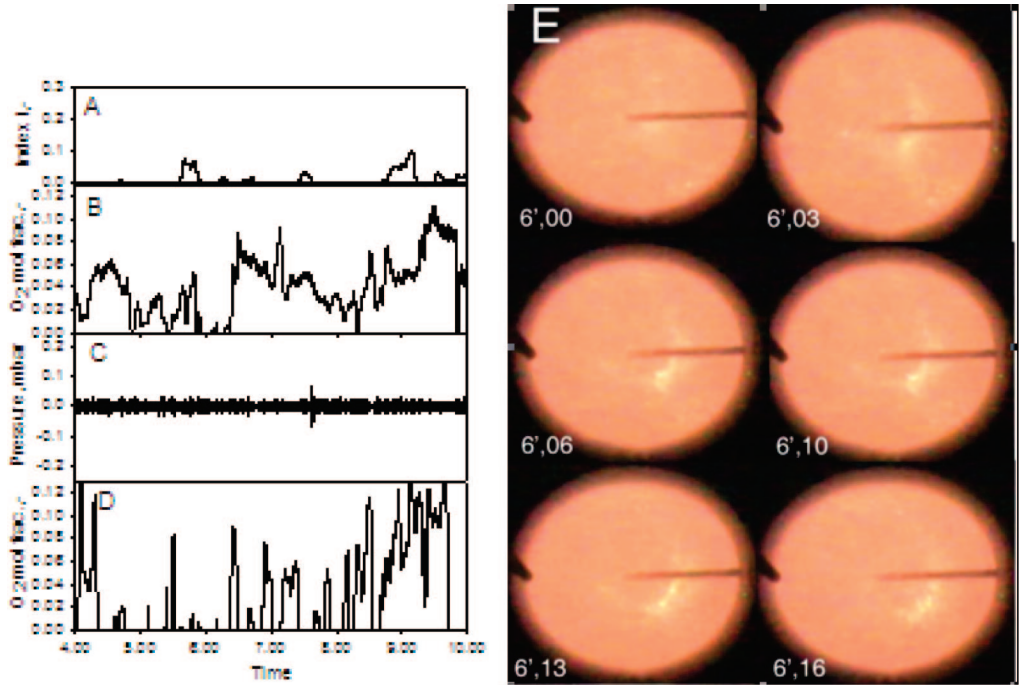

Figure 9. Time-resolved pressure, oxygen concentration, and luminosity index signals and sequence of frames (test 4, $T = 800$ °C): (A) luminosity index Ψ, (B) O_2 concentration in the splash zone, (C) high-pass filtered pressure in the freeboard, (D) O_2 concentration in the bed, and (E) sequence of frames representing the bed surface.

The V-statistic analysis,[22] a technique for the measurement of the length of cyclic periodic and nonperiodic behaviors in a time series, has been extensively applied to the acquired signals of pressure, O_2 molar fraction, and luminosity index to detect the presence of cyclical patterns and to study their evolution with the bed temperature. It is recalled here that a maximum in the semi-log plot of the V_n index, as a function of the time length τ_n, corresponds to a characteristic cycle time in the original time series (see the Appendix).

Figure 10 reports the values of the V_n evaluated for the four time series at different bed temperatures. All of the signals show cyclic behaviors, with periods located in a 1 order of magnitude window, i.e., between 0.2 and 2 s. Furthermore, all plots of V_n as a function of τ_n are unimodal, meaning that there is just one cycle time in the original time series. In Figure 10A, V_n is evaluated for the oxygen concentration signals acquired by the zirconia oxide probe placed 70 mm below the bed surface, at different bed temperatures. The figure indicates that the passage of the oxygen-poor bubbles on the zirconia probe has a period time of about 0.27 s and, correspondingly, a frequency of 3.64 Hz; further, Figure 10A clearly highlights that the bubble motion is independent of the bed temperature. In Figure 10B, the

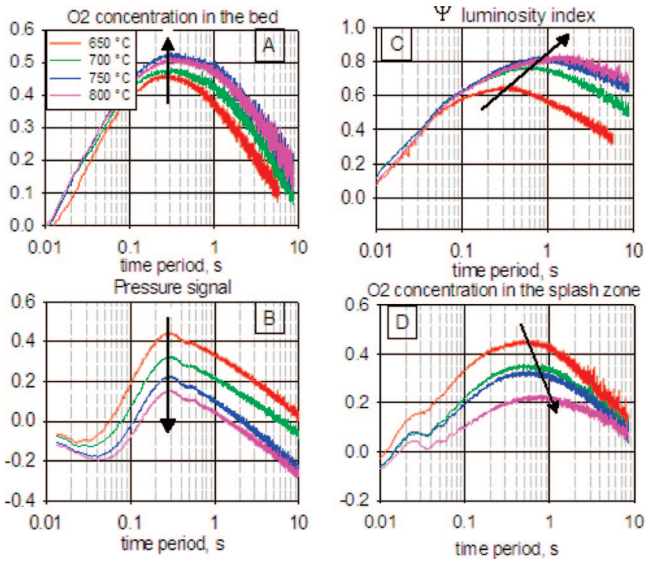

Figure 10. Plots of the V-statistic index V_n for pressure, oxygen concentration, and luminosity index time series at different bed temperatures ($T = 650-800$ °C): (A) O_2 molar fraction in the bed, (B) pressure in the freeboard, (C) luminosity index Ψ, and (D) O_2 molar fraction in the splash zone.

Table 2. Values of the Largest Lyapunov Exponent Estimated for Pressure, Oxygen Concentration, and Luminosity Index Signals at Different Bed Temperatures

test number	T (°C)	pressure signal (s^{-1})	O_2 molar fraction in the bed (s^{-1})	luminosity index Ψ (s^{-1})	O_2 molar fraction in splash zone (s^{-1})
1	650	0.125	0.119	0.132	0.03
2	700	0.125	0.123	0.03	0.04
3	750	0.127	0.118	0.028	0.061
4	800	0.126	0.128	0.033	0.058

V-statistic is reported for the freeboard pressure data. Again, the pressure signals have a constant time period with respect to the bed temperature, and its value is just the same as above (i.e., about 0.27 s). By comparing parts A and B of Figure 10, it can be argued that the generation of a micro-explosion, detected by the pressure transducer, is directly correlated to the rise of the fuel-generated bubble inside the bed. In Figure 10C, V_n is evaluated for the luminosity index; in this case, the cycle period is not constant with temperature. For a bed temperature of 650 °C, the period that is characteristic of bed-surface flashing is about 0.3 s, the same of the pressure and in the bed oxygen concentration. In contrast, when the bed temperature is increased, this period grows up to about 1 s, meaning that less and less light-emitting events are detected by the video recording of the bed surface.

The micro-explosions are directly correlated to the rise of fuel-rich bubbles inside the bed as suggested by comparing parts A and B of Figure 10. Because the in-bed O_2 concentration, pressure, and Ψ signals all exhibit the same cycle period of 0.27 s at 650 °C, it can be argued that a micro-explosion is always correlated to a fuel-generated (hence, oxygen-poor) bubble, more precisely to its appearance in the upper bed part and the subsequent eruption. Furthermore, at 650 °C, the micro-explosions take place always at the bed surface.

Figure 10D reports the V-statistic for the O_2 concentration in the splash zone. The analysis of the Figure 10D shows that (i) fluctuations in the oxygen signal acquired in the splash zone cannot be correlated to the micro-explosive events, because their periods are always higher than the characteristic cycle time of the pressure signal; (ii) the fluctuation period decreases down to 0.5 s when the bed temperature is lowered, with a trend to approach the characteristic period of micro-explosions (0.27 s in Figure 10B).

Because the application of the V-statistic analysis to the acquired signals has proven that all of the signals show a cyclic behavior, the largest Lyapunov exponent has been evaluated as suggested by Peters[22] for each time series with TSTOOL,[24] a MatLab-based software package implementing an algorithm proposed by Wolf et al.,[25] to investigate the nature of those cycles. We recall here that, when the largest Lyapunov exponent λ_1 is positive, the system is said to be chaotic and shows sensitive dependence on initial conditions. Further, λ_1 is an intrinsic characteristic of the chaotic system; this means that if two signals, measurements of two variables of a system, depend upon the same chaotic event, their largest Lyapunov exponents are equal.

In Table 2, the estimates of the largest Lyapunov exponent are reported for the pressure, oxygen molar fractions, and luminosity index signals, during the above-mentioned biodiesel combustion tests at different bed temperature (see Table 1). In all of the cases, the largest exponent is positive, showing that all of the signals are chaotic. Daw and Hallow[23] proved that the fluid dynamics of a bubbling fluidized bed has a chaotic behavior. Therefore, it is reasonable that the combustion of liquid fuels in a fluidized bed shows a chaotic behavior, being itself dependent upon mixing and segregation of the chemical species inside the bed and, in turn, correlated to the bed fluid dynamics.

A comparison of the values assumed by the largest Lyapunov exponent for the different signals confirms the findings already highlighted by the V-statistic analysis. At a bed temperature of 650 °C, the pressure in the freeboard, the O_2 concentration in the bed, and the luminosity index have the same value of the largest Lyapunov exponent, with those signals being different measurements of the same chaotic phenomenon. It means that the approach of a fuel-rich bubble to the bed surface, detected by the zirconia probe below the bed surface, the generation of a micro-explosion, and the detection of a flash at the bed surface are correlated. This reinforces the previous statement that at 650 °C the micro-explosion takes place at the bed surface as a consequence of the eruption of a fuel-generated bubble.

When the bed temperature increases, the Lyapunov exponents of the in-bed O_2 concentration and pressure signals remain constant, whereas the exponent relative to Ψ decreases considerably. Hence, the luminosity index is not representative anymore of the chaotic phenomenon still pinpointed by the in-bed O_2 concentration and pressure signals. This supports the statement that the location of micro-explosions moves deeper into the bed from its surface. In other words, an ignition mechanism of hydrocarbon and pyrolyzed species (that is the origin of micro-explosions) still occurs, but because of the effect of the higher bed temperature, it takes place earlier inside the bed, i.e., during the rise of fuel-rich bubbles and before their approach to the bed surface. As a consequence, micro-explosions are visually undetectable but still occurring inside the bed, as it was the case discussed by Zukowski[13] for the methane−air system.

The Lyapunov exponents of the O_2 molar fraction in the splash zone are still positive, but 1 order of magnitude lower

(23) Daw, C. S.; Halow, J. S. Fluidized processes. *AIChE Symp. Ser.* **1992**, *88* (289), 61−69.
(24) TSTOOL User Manual Version 1.11. http://www.physik3.gwdg.de/tstool, Gnu Public License, 2007.
(25) Wolf, A.; Swift, J. B.; Swinney, L.; Vastano, J. A. *Physica D* **1985**, *16*, 285–317.

than those of the in-bed O_2 concentration and pressure signals. This confirms the previous statement that fluctuations in the oxygen molar fraction in the splash zone are not correlated to the micro-explosive events.

Conclusions

An innovative technique was presented for the analysis and the mechanistic interpretation of the micro-explosive regime in the low-temperature (T < 800 °C) fluidized combustion of in-bed injected liquid fuels. It consists of the comparison of oxygen concentration measured by zirconia-based probes at different heights in the bed and in the splash region, pressure signals measured in the freeboard and purposely filtered, and video frames of the bed surface recorded and purposely worked out.

A qualitative analysis of the signals, acquired during the combustion of biodiesel at minimum fluidization, has proven that the developed technique is a valid tool to detect the occurrence of a localized micro-explosion, despite the small portion of the data series used for its application.

A main part of the work has been devoted to the objective of localizing the micro-explosions in the system and providing a sound explanation for such localization. The application of the integrated diagnostic technique to the fluidized combustion of biodiesel at minimum fluidization has clearly proven that, for a bed temperature of 650 °C, the micro-explosions take place just at bubble eruption at the bed surface. The application of the V-statistic analysis has fully confirmed such a finding because it has demonstrated that a micro-explosion is directly correlated to the rise of fuel-rich bubbles inside the bed. When the bed temperature is above 650 °C, the location of micro-explosions is inside the bed and moves deeper and deeper into it, with the bed temperature increasing up to about 800 °C.

The largest Lyapunov exponent, which has been evaluated for each data series, takes values greater than zero in all cases, demonstrating that the system under study is dynamic and chaotic in its nature. The discussion of the largest Lyapunov exponents fully confirms the findings highlighted by the V-statistic analysis, despite the fact that it is a completely independent investigation tool. The chaotic behavior is not surprising from a physical standpoint; the combustion mechanism involving the reacting chemical species relies on mixing and segregation, and in turn, these latter are influenced by the bubbling bed fluid dynamics, which is well-proven to be chaotic.

Acknowledgment. This work has been carried out under the 2003 MIUR-PRIN financial support. The authors are thankful to Prof. Eliseo Ranzi for his valuable review of L. Ferrante's thesis work and Mr. Antonio Cante for his support for experimental activity.

Appendix

Cycle Detection and Characterization. . This section will explain a method for the detection of cycles originally proposed by Hurst[26] and its evolution, i.e., the V-statistic analysis.[22] Both the methods have been used for the analysis of the cyclic behaviors in fluidized beds.[27−29]

Hurst's Rescaled Range Analysis. . Hurst[26] developed a method based on his studies of long-term water storage to analyze cyclic data collected over time. Hurst applied his technique directly to a set of originally discrete data; in our work, we will apply the technique to a time series that is constructed from "increments" derived from the original data set.

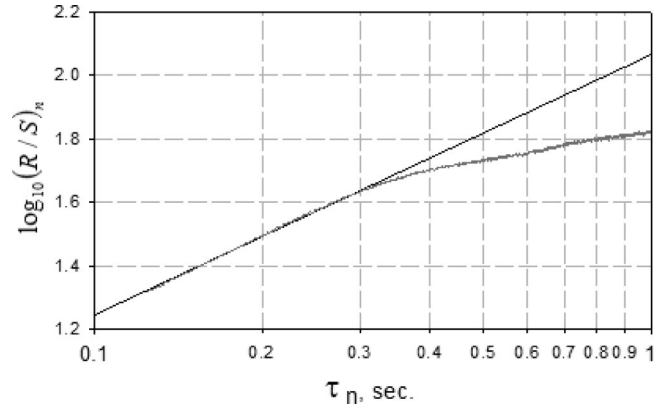

Figure 11. Example from Ferrante[21] of the average rescaled range plot as a function of the time length of the subperiod τ_n for the freeboard pressure signals.

The sequential steps for the application of the Hurst technique to a data set containing $(L + 1)$ elements M_i are reported below:

1. Convert the time-ordered data set of elements M_i into a new series of increments N_i of length L

$$N_i = M_{i+1} - M_i, \quad i = 1, 2, ..., (L)$$

2. Divide the new time series into A intervals of length n, called "subperiods". The element of the ath subperiod I_a (a = 1,..., A) is labeled $N_{k,a}$ (with k = 1,..., n).

3. For each subperiod I_a of length n

a. calculate the average for this subperiod

$$\mu_a = \frac{1}{n}\sum_{k=1}^{n} N_{k,a}$$

b. calculate the standard deviation for this subperiod

$$S_a = \sqrt{\frac{1}{n-1}\sum_{k=1}^{n}(N_{k,a} - \mu_a)^2}$$

c. calculate the accumulated departure from the average

$$X_{k,a} = \sum_{i=1}^{k}(N_{i,a} - \mu_a) \quad k = 1, 2, ..., n$$

d. determine the minimum, $\min(X_{k,a})$, and the maximum, $\max(X_{k,a})$, of the accumulated departure values over the subperiod I_a

e. calculate the range over the subperiod I_a

$$R_a = \max(X_{k,a}) - \min(X_{k,a})$$

f. calculate the rescaled range for subperiod I_a

$$(R/S)_a = R_a/S_a$$

4. Average over all of the A subperiods

a. calculate the average range R_n

$$R_n = \frac{1}{A}\sum_{a=1}^{A} R_a$$

b. calculate the average rescaled range $(R/S)_n$

$$(R/S)_n = \frac{1}{A}\sum_{a=1}^{A}(R/S)_a$$

(26) Hurst, H. E. *Trans. Am. Soc. Civ. Eng.* **1951**, *116*, 770–780.
(27) Kang, Y.; Ko, M. H.; Kim, S. D.; Yashima, M.; Fan, L. T. *AIChE J.* **1996**, *42*, 1164–1169.
(28) Karamavruc, A. I.; Clark, N. H. *Powder Technol.* **1997**, *90*, 235–244.
(29) Briens, L. A.; Briens, C. L. *AIChE J.* **2002**, *48* (5), 970–980.

Repeating steps 2−4 for various values of the subperiod length n (and, hence, the number A of intervals), one obtains a new data set containing $(R/S)_n$, ordered according to n. Therefore, the variation of the average rescaled range $(R/S)_n$ with n can be investigated.

With reference to the time series analyzed in this work, it was preferred to report the variation of $(R/S)_n$ as a function of the characteristic time length of the subperiod τ_n rather than n. With f being the data sampling frequency of the original time series, the time length τ_n of the subperiod is directly proportional to n and the sampling period, f^{-1}: $\tau_n = n/f$.

If the time series exhibits cyclic behavior, then the $\log_{10}-\log_{10}$ plot of $(R/S)_n$ versus τ_n will not be a single straight line. The break point in the straight line slope corresponds to the characteristic cycle time.[22] For example, Figure 11 shows the $\log_{10}-\log_{10}$ plot obtained by applying the Hurst's rescaled range analysis to a time series of pressure data acquired by Ferrante[21] during the low-temperature fluidized combustion of biodiesel; in this case, a characteristic cycle time $t_c = 0.35$ s is estimated.

Generally, cycle times obtained in this way are only approximate estimates. A problem when using Hurst's rescaled range analysis is that it is very difficult to determine the exact location of the break in the $\log_{10}-\log_{10}$ plots of $(R/S)_n$ versus τ_n. Further, if the system under study is chaotic in its nature, nonperiodic cycles exist; these cycles have an average duration, but the exact duration of a future cycle is unknown.[22]

In addition, for the characterization of the time series, it is possible to take into consideration the value of the average range R_n just in correspondence of the break point of the $\log_{10}-\log_{10}$ plot of $(R/S)_n$ versus τ_n. Actually, R_n is a measure of the fluctuation of the original signal with respect to its average value, and larger values of R_n pinpoint signals with wider fluctuations.

V-statistic. . Peters[22] proposed the V-statistic as a further tool to detect cyclic behavior. The V-statistic is a modification of Hurst's rescaled range analysis, which may allow for the location of a break of the $\log_{10}-\log_{10}$ plot of $(R/S)_n$ versus τ_n to be more clearly identified.

The V-statistic index is calculated by adding a fifth step in the sequence of the evaluation of the rescaled range explained in the previous section

5.

$$V_n = \frac{(R/S)_n}{\sqrt{n}}$$

Again, by considering various values of the subperiod length n (and, hence, the number A of intervals and the time length τ_n), one obtains a new data set containing V_n as a function of n and its variation with n or τ_n can be investigated.

A maximum in the plot of V_n as a function of $\log_{10}(\tau_n)$ corresponds to a cycle time in the original time series. Multiple maxima indicate the occurrence of multiple cycles of different time lengths, with each cycle time being found just in correspondence of a peak. As an example, Figure 12 shows the semi-log plot of the V-statistic index for the same time series of Figure 11.

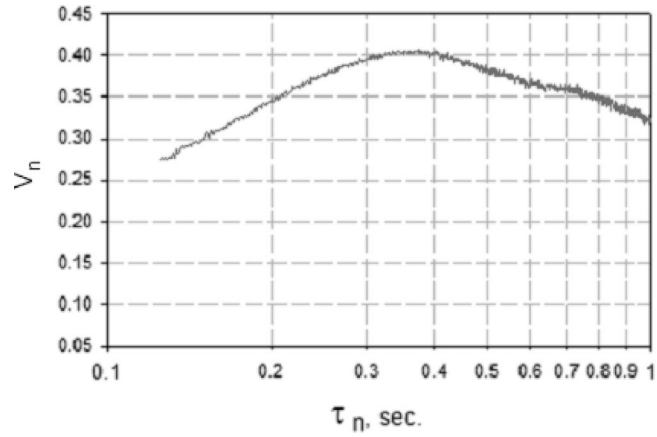

Figure 12. V-statistic index V_n as a function of the time length of the subperiod τ_n for the pressure signals acquired by Ferrante.[21]

Nomenclature

A = number of subperiods in the time series
c = sound velocity in air, m/s
d_t = fluidized bed diameter, m
e = air excess factor
f = sampling frequency in the time series, Hz
F = Faraday constant, C/mol
H_{mf} = static bed height, m
I_a = generic subperiod in a time series
L = number of elements in a time series
L_t = waveguide tube length, m
M_i = generic element in a time series
n = number of elements in a subperiod
N_i, $N_{k,a}$ = incremental element in a time series
R = universal gas constant, J K^{-1} mol^{-1}
R_a = range over the subperiod I_a
R_n = average range over the time series
$(R/S)_a$ = rescaled range over the subperiod I_a
$(R/S)_n$ = rescaled range over the time series
S_a = standard deviation in the subperiod I_a
t = time, s
t_c = cycle time in the time series, s
T = temperature, °C
u_0 = dispersion air velocity at the fuel nozzle, m/s
U = superficial fluidization velocity, m/s
V = electromotive force, mV
V_n = V-statistic index of the time series
$X_{k,a}$ = accumulated departure from the mean in the subperiod
y = volumetric or molar fraction

Greek Symbols
λ_1 = largest Lyapunov exponent of the time series, s^{-1}
μ_a = mean in the subperiod
τ_n = time length of the subperiod, s
Ψ = luminosity index

Subscripts
a = counter of subperiods in a time series
i = element counter in a time series
k = element counter in a time series
mf = minimum fluidization
O_2 = oxygen
ref = reference value

EF800246W